PAPER

Simultaneous catalytic oxidation of Hg^0 and AsH_3 over Fe–Ce co-doped TiO_2 catalyst under low temperature and reducing atmosphere

Huijuan Yu,[ab] Yingjie Zhang, *[ab] Hong Quan,[ab] Dan Zhu,[a] Shaohua Liao,[a] Cuiping Gao,[a] Rongbin Yang,[c] Zhenyu Zhang[c] and Qiang Ma[d]

The Fe–Ce bimetal oxide-doped titanium dioxide composite was synthesized by the sol–gel method and the performance of the catalyst was investigated for the removal of Hg^0 and AsH_3 from yellow phosphorus flue gas under different conditions. Brunauer–Emmett–Teller (BET) analysis, high-resolution transmission electron microscopy (HR-TEM), X-ray diffraction (XRD), and X-ray photoelectron spectroscopy (XPS) were used to characterize the crystal structure and morphology of the structure, and the mechanisms for removing Hg^0 and AsH_3 from flue gas by catalytic oxidation were deduced. The results showed that the optimal calcination temperature of the Fe_5Ce_5Ti catalyst was 500 °C, and the optimal pH of the sol was 6. Under these conditions, the penetration adsorption capacity of the Fe_5Ce_5Ti catalyst for the removal of AsH_3 and Hg^0 was 385.5 mg g^{-1} and 2.178 mg g^{-1}, respectively. According to characterization analysis, Fe and Ce are the main active components in the removal of Hg^0 and AsH_3, and the mixed oxides of Fe and Ce have a synergistic effect on the surface of the mixed oxide-doped catalyst, which can improve the dispersion of the active component on the surface of the catalyst, and then improve the removal efficiency of Hg^0 and AsH_3.

1. Introduction

Atmospheric heavy metal pollution is characterized by wide coverage, strong migration capacity and high biotoxicity,[1,2] and its main source is anthropogenic emissions from the atmosphere. According to estimates, the annual emissions of elemental mercury (Hg^0) and arsenic (AsH_3) have been as high as 695.1 tons and 2529.0 tons, respectively, and with industrial development and energy consumption, the anthropogenic emissions of heavy metals are on the rise.[3] The chemical industry often uses yellow phosphorus as a basic chemical raw material. During the production of yellow phosphorus, a large amount of flue gas is generated, which contains Hg^0 and AsH_3,[4] and it can cause pollution to the atmosphere, soil and water.[5]

Mercury is one of the most toxic heavy metals in the environment; its main forms are mercury oxide (Hg^{2+}), particulate mercury (Hg^P) and elemental mercury (Hg^0) in the atmosphere.[6]

Normally, Hg^{2+} and Hg^P in the atmosphere can be deposited on the ground surface by dry and wet deposition, and in industry, these can be removed by wet scrubbing and dust removal devices. In contrast, it is difficult to capture Hg^0 by equipment due to its stable chemical nature and it can easily enter the geochemical cycle,[7,8] causing harm to human health through the food chain.[9,10]

Arsenic (As) belongs to the highly toxic group of metals and exists in the environment in many different chemical forms,[11] which are divided into As(v) and As(III) by the difference in chemical valence, where As(III) is about 60 times higher than As(v) and is extremely hazardous to organisms[12,13] As and Hg^0 are absorbed by the human body and combine easily with hydrogen sulfide or bisulfide to inhibit cellular respiration and normal cellular metabolism.

The present methods for the removal of Hg^0 and AsH_3 from gases mainly involve adsorbent removal,[14–17] catalytic oxidation[18–20] and advanced oxidation.[21–23] Podak[24] *et al.* found that fluorine-modified activated carbon has a strong adsorption capacity for Hg^0. Li[25] *et al.* used Ce–Mn mixed oxide-loaded activated carbon to remove Hg^0 at a low temperature with a removal efficiency of up to 94%. Quinn[26] *et al.* showed the excellent adsorption of AsH_3 by the isovolumetric impregnation of roasted commercial activated carbon with copper nitrate. Poulston[27] *et al.* used the noble metal Pb as the active component and the results showed that the Pb/Al_2O_3 could effectively adsorb Hg from the flue gas. The adsorption method has been

[a]College of Agriculture and Biological Science, Dali University, No. 2, Hong Sheng Road, Dali 671000, China. E-mail: hjyu_yhj@163.com; yjzhang_dlu@163.com; hongq_9795@163.com; dzhudali@163.com; liaoshaohua@foxmail.com; gaocp_dlu@163.com; Tel: +86 15687786161

[b]Key Laboratory of Ecological Microbial Remediation Technology of Yunnan Higher Education Institutes, Dali University, Dali 671000, China

[c]College of Engineering, Dali University, Dali 671000, China. E-mail: yangronbin@126.com; 276442688@qq.com

[d]School of Architecture and Civil Engineering, Chengdu University, Chengdu 610106, China. E-mail: maqiang@cdu.edu.cn

studied by numerous scholars because of its excellent ability to remove heavy metals. However, it still has deficiencies such as poor thermodynamic stability and low mixability. Noble metal catalysts cannot be used on a large scale due to their high cost but transition metals and their oxides, and rare earth metals and their oxides have become hot spots of interest for researchers because of their superior removal effect and lower cost.

Cerium Oxide (CeO_2) is a rare earth metal oxide with extremely strong redox and oxygen storage properties, often used as an additive or co-catalyst to improve reaction activity and to a large extent to enhance anti-aging and anti-poisoning ability. In the redox process, Ce^{4+}/Ce^{3+} will produce unstable oxygen vacancies and large amounts of oxygen with high mobility during the mutual transformation. It can adsorb trace amounts of O_2 in the gas phase to replenish the consumed oxygen on the catalyst surface and improve the catalytic performance of the catalyst. Part of the industrial exhaust contains traces of oxygen, so CeO_2-based catalysts are commonly used in the field of industrial waste gas heavy metal removal. Zhao[28] *et al.* explored that CeO_2-based catalysts were effective in removing Hg^0 from flue gas. Some researchers[29,30] prepared CeO_2–TiO_2 composite catalysts and concluded that there is a strong interaction between Ce and Ti, and the high dispersion of CeO_2 is the main reason for the superior catalytic activity of the catalysts. Liu[31] *et al.* prepared $FeTiO_X$ composite oxide catalysts with high catalytic activity and found that the interaction between titanium and iron atoms can cause the active material to be highly dispersed in the form of micro-crystals with strong Brønsted and oxidation ability on the catalyst surface. It was found that the oxygen storage and oxygen release properties of CeO_2 were significantly improved due to the presence of Fe^{3+} with a relatively small ionic radius and low valence, and it also facilitated the creation of more sites on the surface of CeO_2 for heavy metal ion binding, which effectively enhanced the redox properties of CeO_2. Metal or metal oxide type catalysts have strong catalytic effects due to their renewable and high conversion rates, so they were combined as catalysts.[32] TiO_2 has a strong stabilization type and low cost, and it is widely used in the field of catalysis, so they were combined to investigate their effects on the removal of Hg^0 and AsH_3 from yellow phosphorus flue gas. In summary, by doping CeO_2 with other substances, the specific surface area of the catalyst is influenced to induce a wider distribution of active components, enhance oxygen vacancy and lattice oxygen mobility, and achieve the purpose of improving the catalyst performance, which effectively solves the problems of high processing cost and imperfect processes of the existing technology.

There has been some development of yellow phosphorus flue gas purification and resource utilization technology but little has been reported on the removal of heavy metals Hg^0 and AsH_3, which have a great influence on the catalysis of yellow phosphorus flue gas purification. In this study, we prepared Fe and Ce doped TiO_2 nanocomposites and explored catalysts for the highly selective removal of Hg^0 and AsH_3 from yellow phosphorus flue gas by changing the reaction conditions, and characterizing the materials by BET, HR-TEM, XRD, and XPS for

microscopic analysis. This is expected to elucidate the removal mechanism through a combination of macroscopic and microscopic analyses and establish a multidimensional risk evaluation mechanism to achieve the efficient removal of Hg^0 and AsH_3 from flue gas.

2.   Experimental

2.1.   Catalyst preparation

Fe_5Ce_5Ti and TiO_2 were prepared at different sol–gel pH values, and the metal oxide catalysts $Fe_{10}Ti$, $Ce_{10}Ti$ and Fe_5Ce_5Ti were prepared at the optimum pH by the sol–gel method. As an example, a 2 g sample of catalyst was prepared as follows.

Solution A: a certain mass of anhydrous citric acid[33] was weighed on an analytical balance and added to 21–24 mL of anhydrous ethanol. The mixture was stirred for 30 min at 30 °C with a magnetic stirrer. After stirring until the solute was completely dissolved, we slowly added 7–8 mL of tetrabutyl titanate and 1.5 mL of acetylacetone, and continued stirring at 30 °C with a magnetic stirrer for 30 min, to obtain a light yellow transparent solution. The solid–liquid ratio of anhydrous citric acid and anhydrous ethanol is 1 : 4, and the volume ratio of anhydrous ethanol and tetrabutyl titanate is 3 : 1.

Solution B: a certain amount of 5 wt% $Ce(NO_3)_3 \cdot 6H_2O$ and 5 wt% $Fe(NO_3)_3 \cdot 9H_2O$ were weighed in a beaker, then 5 mL deionized water, 10 mL anhydrous ethanol and 1 mL HNO_3 were added and stirred until the mixture was uniform.

Under intense agitation, solution B was dropped into A solution at the speed of 1 drop/second, and nitric acid or ammonia water was slowly added to adjust the pH of the sol to 6. A magnetic stirrer was used to continue to stir the solution of suitable pH value until a light yellow translucent sol precursor with a different pH value was obtained. The obtained sol was placed in a thermostatic water bath at 70 °C for 3 h to obtain a wet gel, and then the wet gel was moved to a crucible and dried overnight at 60 °C in a blast drying oven. The temperature was increased and kept at 500 °C for 2 h, then cooled to room temperature to obtain the Fe_5Ce_5Ti catalyst. It was then ground and pressed into tablets, passed through a 40–60 mesh sieve, sealed and stored. Fe_5 and Ce_5 represent the mass fractions of Fe_2O_3 and CeO_2 to the total mass of the Fe_5Ce_5Ti catalyst, respectively.

TiO_2 was prepared by a sol–gel method. The metallic salt precursors of Fe and Ce were not added to solution B, and upon the addition of $Ce(NO_3)_3 \cdot 6H_2O$ or $Fe(NO_3)_3 \cdot 9H_2O$ to solution B, $Ce_{10}Ti$ or $Fe_{10}Ti$ was prepared, respectively. The other steps are the same as above.

2.2.   Catalyst characterization

The Brunauer–Emmett–Teller (BET) method was used to characterize the surface area, pore volume and radius. High-resolution transmission electron microscope (HR-TEM) images were obtained on a JEOL JEM-2100F electron microscope (200 kV accelerating voltage) for morphological characterization of samples. Characterization of the elemental composition of the sample using the X-ray diffraction (XRD) was

carried out on a Bruker D8-Advance XRD system using Cu Kα radiation ($\lambda = 0.1543$ nm) at 2θ values ranging from 10° to 90°, with a step size of 0.02°. The surface chemical state of the samples was determined using X-ray photoelectron spectroscopy (XPS), Thermo ESCALAB 250 Xi, with an Al Kα source (1486.6 eV photons).

The Debye–Scherrer formula was used to calculate the crystal size of TiO_2 grains of Fe_5Ce_5Ti catalysts prepared at different calcination temperatures. The formula is as follows:

$$D_{hkl} = \frac{k\lambda}{\beta \cos \theta}$$

D_{hkl} is the calculated grain size; k is a constant, depending on the shape of the crystal, where $k = 0.9$; λ is the wavelength of Cu Kα X-ray radiation, $\lambda = 1.5418$; β is the half peak width of the diffraction peak of the TiO_2 crystal; θ is the diffraction angle corresponding to the diffraction peak.

2.3. Catalyst activity test

The specific reaction conditions of this chapter are shown in Table 1. In the experiment, the total simulated flue gas flow was 800 mL min^{-1}, the catalyst filling volume was 200 mg, and Hg^0 and AsH_3 inlet concentrations were 400 μg m^{-3} and 50 ppm, respectively. To shorten the experimental reaction time and minimize the relative error in the continuous data collection process, higher concentrations of Hg and As were set at the inlet.

3. Results and discussion

3.1. Catalyst performance

3.1.1. The effects of active components on the removal performance of Hg^0 and AsH_3. In this study, the effects of doping types of active components on the removal efficiencies of Hg^0 and AsH_3 were investigated, and four catalysts, TiO_2, $Fe_{10}Ti$, $Ce_{10}Ti$ and Fe_5Ce_5Ti, were compared. The results are shown in Fig. 1. The maximum removal efficiency of Hg^0 by $Fe_{10}Ti$ was 79.8%, and the maximum removal efficiencies of Hg^0 by $Ce_{10}Ti$ and Fe_5Ce_5Ti were 83.2% and 93.5%, respectively. The removal efficiency of Hg^0 by the bimetallic active component-doped TiO_2 was better than that by the single metal active component-doped TiO_2. Similarly, the removal of AsH_3 showed the same trend, where the Fe_5Ce_5Ti catalyst had the best AsH_3 removal efficiency, while the single metal active component-doped TiO_2 catalyst had a poor AsH_3 removal efficiency. Without the doping of the active component, the catalyst has a poor ability to remove Hg^0 and AsH_3 because only micro-oxygen in the gas phase can oxidize Hg^0 and AsH_3. All the results showed that Fe and Ce were the main active components in the removal of Hg^0 and AsH_3, and the Fe and Ce mixed oxides had a synergistic effect on the surface of the two-component active component-doped catalyst, which could improve the dispersity of the active components on the surface of the catalyst, thus improving the removal ability of Hg^0 and AsH_3. Such a synergistic effect can still occur in the reducing atmosphere, so in the subsequent experiments, the Fe–Ce bimetallic oxide

Table 1 The experimental reaction conditions

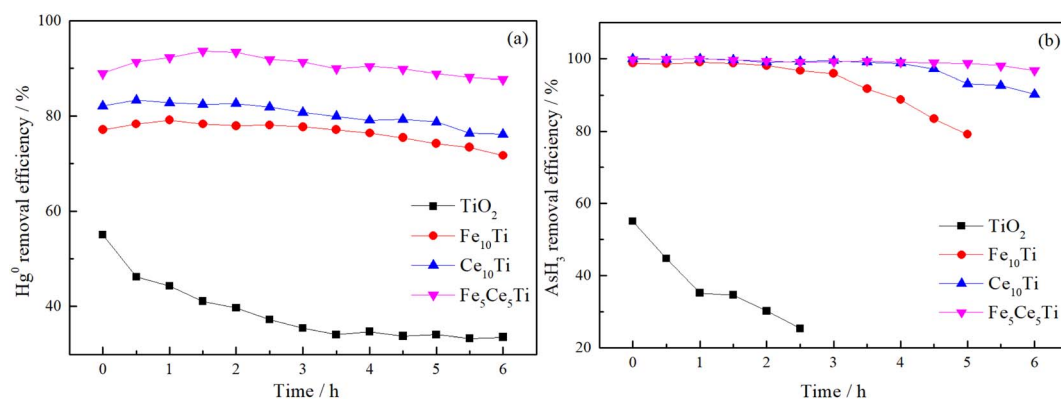| Experiment | Samples | | | | |
	Fe_xCe_yTi	Sol pH	Calcination temperature	Flue gas components	Temperature
1	TiO_2, Fe_5Ce_5Ti, $Fe_{10}Ti$, $Ce_{10}Ti$	6	500 °C	N_2 + 80% CO + 1% O_2 + AsH_3 + Hg^0	150 °C
2	Fe_5Ce_5Ti	6	300–700 °C	N_2 + 80% CO + 1% O_2 + AsH_3 + Hg^0	150 °C
3	Fe_5Ce_5Ti	2, 4, 6, 8, 10	500 °C	N_2 + 80% CO + 1% O_2 + AsH_3 + Hg^0	150 °C
4	Fe_5Ce_5Ti	6	500 °C	N_2 + 80% CO + 1% O_2 + AsH_3 + Hg^0	100–170 °C
5	Fe_5Ce_5Ti	6	500 °C	N_2 + AsH_3 + Hg^0 +77 (CO + O_2)	150 °C

Fig. 1 The effects of active components on the removal efficiencies of Hg^0 (a) and AsH_3 (b) over Fe_xCe_yTi catalysts (total gas flow: 800 mL min^{-1}, catalyst filling capacity: 200 mg, Hg^0: 400 μg m^{-3}, AsH_3: 50 ppm, O_2: 1 vol%, CO: 80 vol%, reaction temperature: 150 °C).

was doped into TiO_2 as the best active component of the catalyst.

3.1.2. The effects of calcination temperature on the removal performance of Hg^0 and AsH_3.

When making a catalyst, its crystal structure and grain size are closely related to the calcination temperature. In this experiment, Fe_5Ce_5Ti catalysts were prepared at 300 °C, 400 °C, 500 °C, 600 °C and 700 °C, respectively,[34] and the removal efficiency of Hg^0 and AsH_3 was investigated. The results are shown in Fig. 2. The removal performance of Hg^0 and AsH_3 at different calcination temperatures is 500 °C > 600 °C > 400 °C > 300 °C > 700 °C, 500 °C > 400 °C > 600 °C > 300 °C > 700 °C. The catalyst prepared at the roasting temperature of 700 °C has the worst effect on removing Hg^0 and AsH_3, which may be due to the sintering of the active component of the catalyst due to the high temperature, thus reducing the active sites and reducing the performance of the catalyst. The catalyst prepared at 500 °C has the best effect of removing Hg^0 and AsH_3, and the calcined Fe and Ce can form a regular crystal structure at this temperature. Anatase and rutile are the two most important crystal structures of TiO_2.[35] When roasted in the temperature range below 800 °C, the crystal phase change order of TiO_2 grains is amorphous, anatase, anatase mixed with rutile, and rutile. In general,

anatase TiO_2 can provide more active sites for the active components of the catalyst and is more suitable as the catalyst carrier. This speculation was also confirmed in the subsequent XRD analysis. Therefore, 500 °C was selected as the optimal calcination temperature for the Fe_5Ce_5Ti catalyst in subsequent experiments.

3.1.3. The effects of sol pH on the removal performance of Hg^0 and AsH_3.

The pH value of the sol has a great influence on the surface morphology and catalytic performance of the catalysts prepared by the sol–gel method.[36] The removal efficiencies of the Fe_5Ce_5Ti catalyst prepared at sol pH of 2, 4, 6, 8 and 10 for Hg^0 and AsH_3 are shown in Fig. 3. When the pH value of the sol was 2, the removal efficiency of Hg^0 was the lowest, which was only 72.5%, and the removal efficiency was up to 93.6% when the pH was 6. However, when the pH was 8 and 10, the removal efficiency of Hg^0 decreased. The effect of sol pH on the AsH_3 removal efficiency is the same as that of Hg^0. The removal efficiency of AsH_3 was the best when the pH of the sol was 6, and the removal efficiency of AsH_3 was 96.8% when the reaction was 6 h. The removal efficiency of AsH_3 was the worst when the pH of the sol was 2, and the removal efficiency decreased to 88.2% when the reaction time was 3.5 h. In the process of catalyst preparation, the sol pH had a great influence on the surface
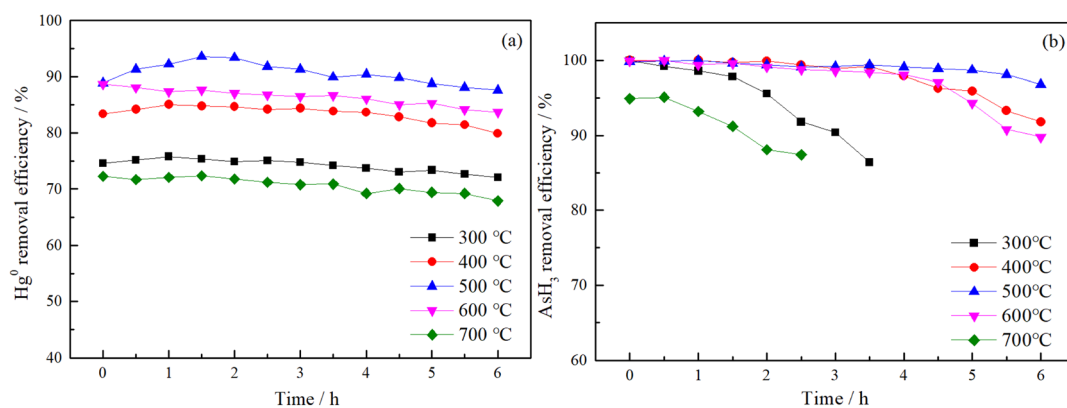

Fig. 2 The effects of the calcination temperature on the removal efficiencies of Hg^0 (a) and AsH_3 (b) over Fe_5Ce_5Ti catalysts (total gas flow: 800 mL min^{-1}, catalyst filling capacity: 200 mg, Hg^0: 400 μg m^{-3}, AsH_3: 50 ppm, O_2: 1 vol%, CO: 80 vol%, reaction temperature: 150 °C).
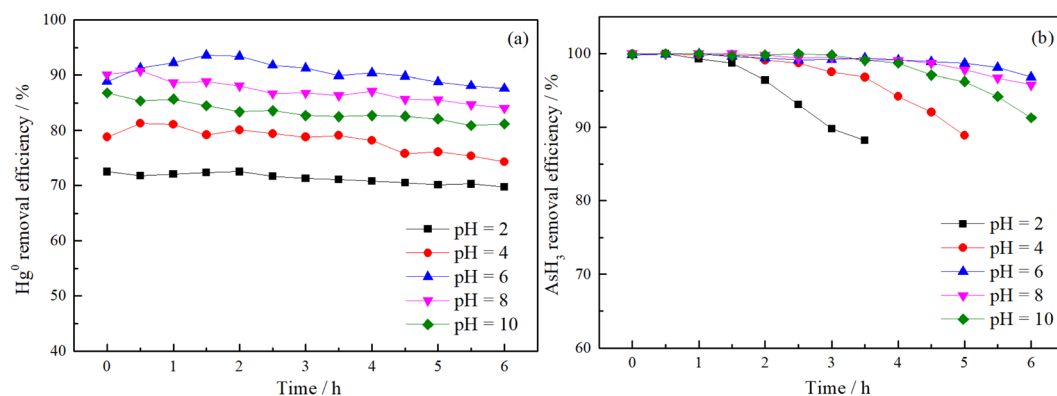

Fig. 3 The effects of the sol pH on the removal efficiencies of Hg^0 (a) and AsH_3 (b) over Fe_5Ce_5Ti catalysts (total gas flow: 800 mL min^{-1}, catalyst filling capacity: 200 mg, Hg^0: 400 μg m^{-3}, AsH_3: 50 ppm, O_2: 1 vol%, CO: 80 vol%, reaction temperature: 150 °C).

morphology and microstructure of the prepared Fe_5Ce_5Ti catalyst, which further affected the removal efficiency of Hg^0 and AsH_3. Sol pH is one of the important parameters for the preparation of catalysts by the sol–gel method. The optimum sol pH value of the Fe_5Ce_5Ti catalyst is 6.

3.1.4. The effects of reaction temperature on the removal performance of Hg^0 and AsH_3. To determine the optimal reaction temperature for the simultaneous removal of Hg^0 and AsH_3, the Fe_5Ce_5Ti catalyst was used to carry out a series of experiments in the temperature range of 100–170 °C, and the results are shown in Fig. 4. The removal efficiency of Hg^0 increased with the increase in temperature in the range of 100 °C to 150 °C, and decreased when the temperature was higher than 150 °C. This phenomenon can be explained by the decrease in the chemisorption of Hg^0 and the desorption of HgO on the catalyst surface at high temperatures. The removal efficiency of AsH_3 increased with the increase in temperature. When the reaction temperature was 170 °C, the removal efficiency of AsH_3 was only slightly better than that of AsH_3 at 150 °C. However, the reaction temperature at 170 °C is close to the decomposition temperature of AsH_3 and the activation temperature of CO oxidation by CeO_2.[37] In consideration of safety and practical industrial applications, the reaction temperature should be set below 180 °C. The higher temperature enhanced the catalytic oxidation, and Hg^0 and AsH_3 would be oxidized to high-valence states on the surface of the catalyst. This result was confirmed in the subsequent characterization analysis. The Fe_5Ce_5Ti catalyst has the best Hg^0 removal efficiency and high AsH_3 removal efficiency at 150 °C. The removal efficiency of Hg^0 by the Fe_5Ce_5Ti catalyst reached 93.6%, and the removal efficiency of AsH_3 was still as high as 96.8% after 6 h of reaction. Therefore, 150 °C was considered to be the best reaction temperature for the simultaneous removal of Hg^0 and AsH_3, and it was set as the default reaction temperature in subsequent experiments.

3.1.5. The effects of O_2 concentration on the removal performance of Hg^0 and AsH_3. As an important part of flue gas components, oxygen concentration has a significant impact on the simultaneous removal of Hg^0 and AsH_3, and the removal

efficiencies of Hg^0 and AsH_3 under aerobic and anaerobic conditions are significantly different, as shown in Fig. 5. The removal efficiency of AsH_3 by Fe_5Ce_5Ti catalyst is poor in the absence of oxygen, and the removal efficiency of AsH_3 dropped to 88.4% after 3 h of reaction. When 0.5% O_2 was added to the gas phase, the removal efficiency of AsH_3 increased significantly. The removal efficiency of Fe_5Ce_5Ti catalyst for Hg^0 in the absence of oxygen is also poor, being only 60.3%; when 0.5% O_2 was added to the gas phase, the removal efficiency of Hg^0 increased to 86.9%. This may be because the surface oxygen of the catalyst is rapidly consumed in the absence of oxygen and cannot be replenished. Oxygen in the gas phase can supplement the lattice oxygen and chemisorbed oxygen consumed in the oxidation of Hg^0 and AsH_3 by the catalyst in the micro-oxygen condition. With the increase of the O_2 concentration from 0.5% to 1% in the gas phase, the removal efficiency of Hg^0 and AsH_3 did not improve significantly. The results show that the catalyst has a high removal efficiency for Hg^0 and AsH_3 in micro-oxygen conditions, and a 1% O_2 concentration is sufficient for the simultaneous removal of Hg^0 and AsH_3.

3.2. Catalyst characterization

The BET, HR-TEM, XRD and XPS methods were used to determine the mechanisms of the effects of the removal mechanism of Hg^0 and AsH_3 by Fe_5Ce_5Ti.

3.2.1. BET analysis. The physical properties of the Fe_5Ce_5Ti catalysts prepared by different sol pH, including the BET surface area, pore volume and pore radius, are summarized in Table 2. The results show that the pore volume and average pore size of the five catalysts increased with the increase of the pH value of the sol. When the pH value of the sol was 6, the Fe_5Ce_5Ti catalyst had the largest specific surface area of 109.543 m^2 g^{-1}; because this value of the sol is close to the isoelectric point of TiO_2,[38] it is conducive to the growth of TiO_2 particles and the formation of nanocrystals with large specific surface area. Therefore, the inorganic network structure and surface morphology of materials prepared by the sol–gel method are closely related to the pH value of the sol. In the preparation process of the Fe_5Ce_5Ti catalyst, tetrabutyl titanate was firstly
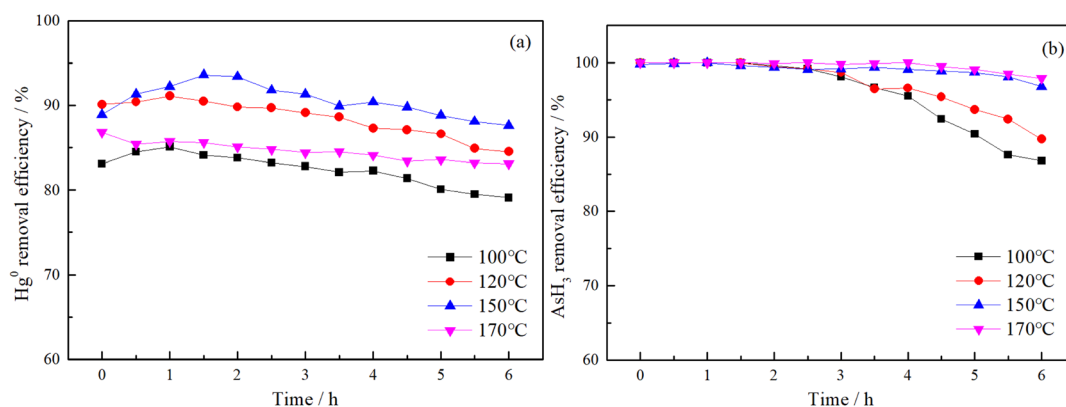

Fig. 4 The effects of the different reaction temperatures on removal efficiencies of Hg^0 (a) and AsH_3 (b) over Fe_5Ce_5Ti catalysts (total gas flow: 800 mL min^{-1}, catalyst filling capacity: 200 mg, Hg^0: 400 μg m^{-3}, AsH_3: 50 ppm, O_2: 1 vol%, CO: 80 vol%, reaction temperature: 100–170 °C).

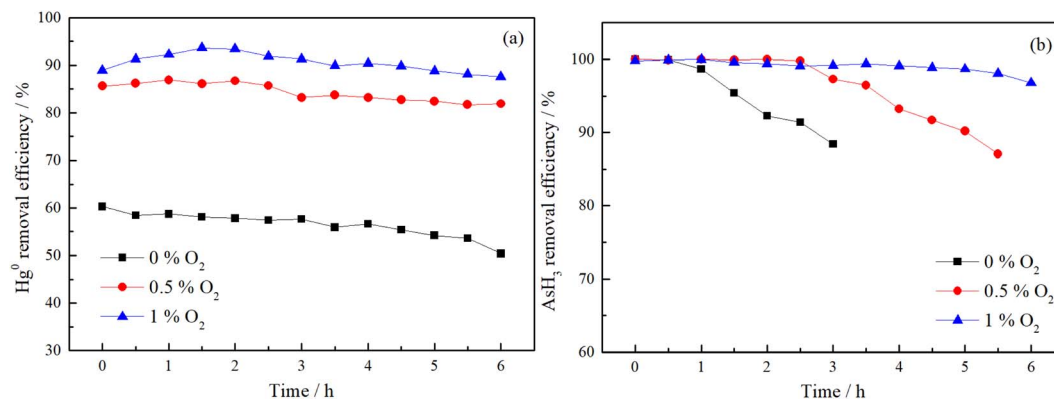**Fig. 5** The effects of O_2 concentration on the removal efficiencies of Hg^0 (a) and AsH_3 (b) over Fe_5Ce_5Ti catalysts (total gas flow: 800 mL min^{-1}, catalyst filling capacity: 200 mg, Hg^0: 400 μg m^{-3}, AsH_3: 50 ppm, O_2: 0–1 vol%, CO: 80 vol%, reaction temperature: 150 °C).

Table 2 BET specific surface, pore volume and pore diameter of different sol pH Fe_5Ce_5Ti catalysts

Sample (sol pH)	Surface area (m^2 g^{-1})	Pore volume (cm^3 g^{-1})	Average pore size (nm)
2	50.505	0.062	3.405
4	83.437	0.089	3.403
6	109.543	0.126	3.450
8	95.145	0.117	3.427
10	95.109	0.105	3.552

hydrolyzed to $Ti(OH)_4$, and then $Ti(OH)_4$ was polymerized and converted into inorganic oxides with reticular structure. The possible reactions are as follows:

$$Ti(O–C_4H_9)_4 + 4H_2O \rightarrow Ti(OH)_4 + 4C_4H_9OH \tag{1}$$

$$Ti(OH)_4 \rightarrow TiO_2 \cdot nH_2O + (2 − n)H_2O \tag{2}$$
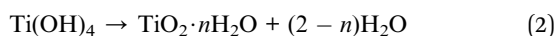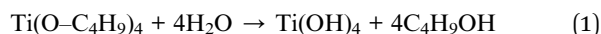
The relative contents of H^+ and OH^- in precursors of different sol pH values affect the binding capacity of Ti^{4+} and OH^-. When the sol pH is less than 6, the precursor solution is acidic, and the stable $Ti(OH)_4$ nucleation cannot occur, resulting in the expansion of the material. With the increase in the pH of the sol, the concentration of OH^- increases and the surface hydroxylation occurs, which is conducive to the polycondensation reaction, so that the hydrolysates agglomerate and the average pore size of the grains increases. The larger specific surface area is beneficial for the dispersion of active components, increasing the number of active points on the catalyst surface, and enhancing the performance of the catalyst.

3.2.2. HR-TEM analysis. HR-TEM images of the Fe_5Ce_5Ti catalyst prepared under different sol pH conditions are shown in Fig. 6; the crystal patterns of Fe_5Ce_5Ti catalysts prepared by different sol pH were observed in the HR-TEM images. The results show that the Fe_5Ce_5Ti catalysts prepared at different sol pH have satisfactory crystal phases. When the sol pH is 2, as shown in Fig. 6(a), the prepared samples have two lattice stripes of 0.321–0.327 nm and 0.350–0.358 nm, which presumably

correspond to the rutile crystal type and anatase crystal type, respectively,[39] and the rutile crystal type is the major type, whereas the anatase crystal content is less. When the pH of the sol was 4, 8 and 10, as shown in Fig. 6(b), (d) and (e), it was assumed that the prepared samples also contained rutile crystals and anatase crystal, and the TiO_2 particles in the prepared Fe_5Ce_5Ti catalyst were mainly anatase crystals, with less rutile crystal content. When the sol pH was 6, as shown in Fig. 6(c), it was inferred that the prepared Fe_5Ce_5Ti catalyst had only anatase crystalline TiO_2 particles, and it was confirmed that the anatase crystal type TiO_2 has optimal potential as a catalyst carrier.[40] Therefore, the Fe_5Ce_5Ti catalyst prepared when the sol pH is 6 had the best surface morphology and TiO_2 particle crystal shape. We used ICP-OES to determine the Fe and Ce contents in Fe_5Ce_5Ti, which were 42.36 mg g^{-1} and 48.02 mg g^{-1}, respectively.

3.2.3. XRD analysis. To explore the relationship between calcination temperature and the crystal structure of the Fe_5Ce_5Ti catalyst and the reason for the influence of calcination temperature on the removal efficiency of Hg^0 and AsH_3, XRD analysis of Fe_5Ce_5Ti catalysts prepared at 300 °C, 400 °C, 500 °C, 600 °C and 700 °C was carried out. XRD patterns are shown in Fig. 7 and Table 3. With the roasting temperature increasing from 300 °C to 500 °C, the characteristic peak of the anatase crystal structure gradually appeared. The diffraction peaks with 2θ values of 25.4°, 38.1°, 48.0°, 54.7°, 62.7° and 76.5° were TiO_2 (PDF21-1272) anatase diffraction peaks. The Fe_5Ce_5Ti catalyst prepared at 300 °C was completely composed of anatase crystals with an average grain size of 8 nm. At this time the XRD pattern of the catalyst had low diffraction peak intensity and small grain size, mainly because the low calcination temperature led to the inadequate crystallinity of TiO_2. The diffraction peak of rutile was not observed in the catalysts prepared at the roasting temperatures of 500 °C and below, and the intensity of the anatase diffraction peak increased with the roasting temperature, which may be due to the thermally induced growth of TiO_2 particles and the increase in the crystallinity of the TiO_2 particles.[41] When the roasting temperature was further increased, the TiO_2 crystal type changed from anatase to rutile, and the higher the roasting temperature, the more obvious the
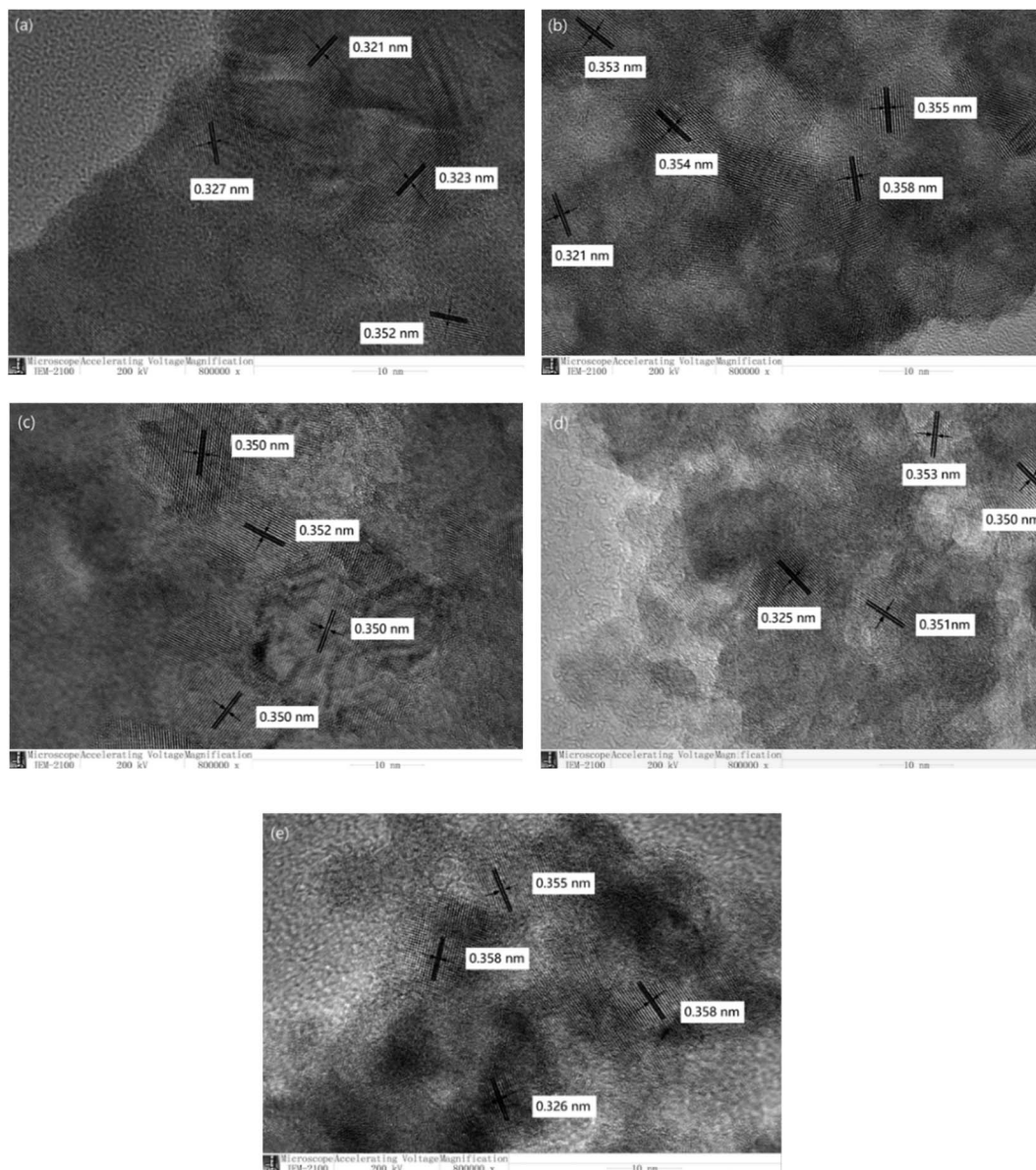
Fig. 6 HR-TEM photographs of Fe$_5$Ce$_5$Ti catalysts prepared with sol pH = 2 (a), 4 (b), 6 (c), 8 (d) and 10 (e).
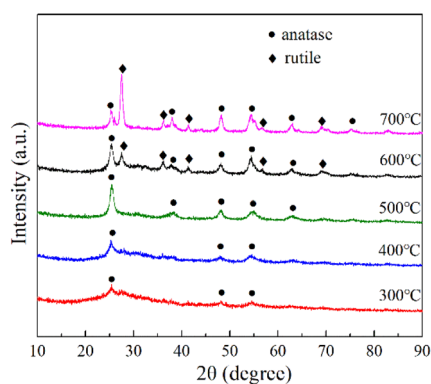

Fig. 7 XRD patterns of Fe$_5$Ce$_5$Ti catalysts at different calcination temperatures.

Table 3 The crystallite forms and sizes of the different calcination temperature Fe$_5$Ce$_5$Ti catalysts

Samples (calcination temperature)	Crystallite size (nm)	
	Anatase	Rutile
300 °C	8.0	—
400 °C	11.2	—
500 °C	10.6	—
600 °C	12.8	14.0
700 °C	15.4	18.3

diffraction peak of rutile, and the grain size also increases. With the increase in roasting temperature, the size of the anatase crystal increased from 8.0 nm to 15.4 nm, and the size of the rutile crystal increased from 14.0 nm to 18.3 nm. The higher

roasting temperature promotes the agglomeration of TiO_2 particles, resulting in the growth of particles and the increase in grain size. However, the diffraction peaks of Fe_3O_4 and CeO_2 were not observed in the XRD patterns, indicating that the oxides of Fe and Ce were evenly dispersed on the surface of TiO_2. Combined with the XRD characterization analysis results and the influence of the Fe_5Ce_5Ti catalyst prepared at different roasting temperatures on the removal performance of Hg^0 and AsH_3 discussed above, 500 °C was selected as the optimal roasting temperature for the Fe_5Ce_5Ti catalyst.

3.2.4. XPS analysis. To confirm the chemical state of the main elements on the surface of the Fe_5Ce_5Ti catalyst before and after the reaction, and the relative content of each element, XPS characterization of O 1s, Fe 2p, Ce 3d, Hg 4f and As 3d was performed on the Fe_5Ce_5Ti catalyst, and the contents of the individual elements after the peaks split were calculated. Fig. 8(a–e) show the XPS spectra of Fe_5Ce_5Ti catalysts; the

proportions of O_α and O_β, Fe^{3+} and Fe^{2+}, Ce^{4+} and Ce^{3+} were calculated from the sum of the areas of different characteristic peaks, as shown in Table 4.

The characteristic peaks detected in the XPS spectrum can be divided into two overlapping peaks corresponding to different forms of oxygen on the catalyst surface. The characteristic peak at 529.8 eV is lattice oxygen, denoting O_α, and the characteristic peak at higher binding energy is chemisorbed oxygen, denoting O_β. The percentage of O_α and O_β on the catalyst surface is denoted as O_α/O_T and O_β/O_T ($O_T = O_\alpha + O_\beta$),[19] respectively. The elements of O_α and O_β are shown in Table 4. Compared with the Fe_5Ce_5Ti catalyst before the reaction, the lattice oxygen content O_α/O_T on the catalyst surface after the reaction decreased from 75.17% to 65.80%. The results show that lattice oxygen is involved in the catalytic oxidation of Hg^0 and AsH_3, and Hg^0 and AsH_3 adsorbed on the surface of the catalyst were oxidized into HgO, elemental As and As_2O_3. The ratio of O_β/O_T adsorbed on
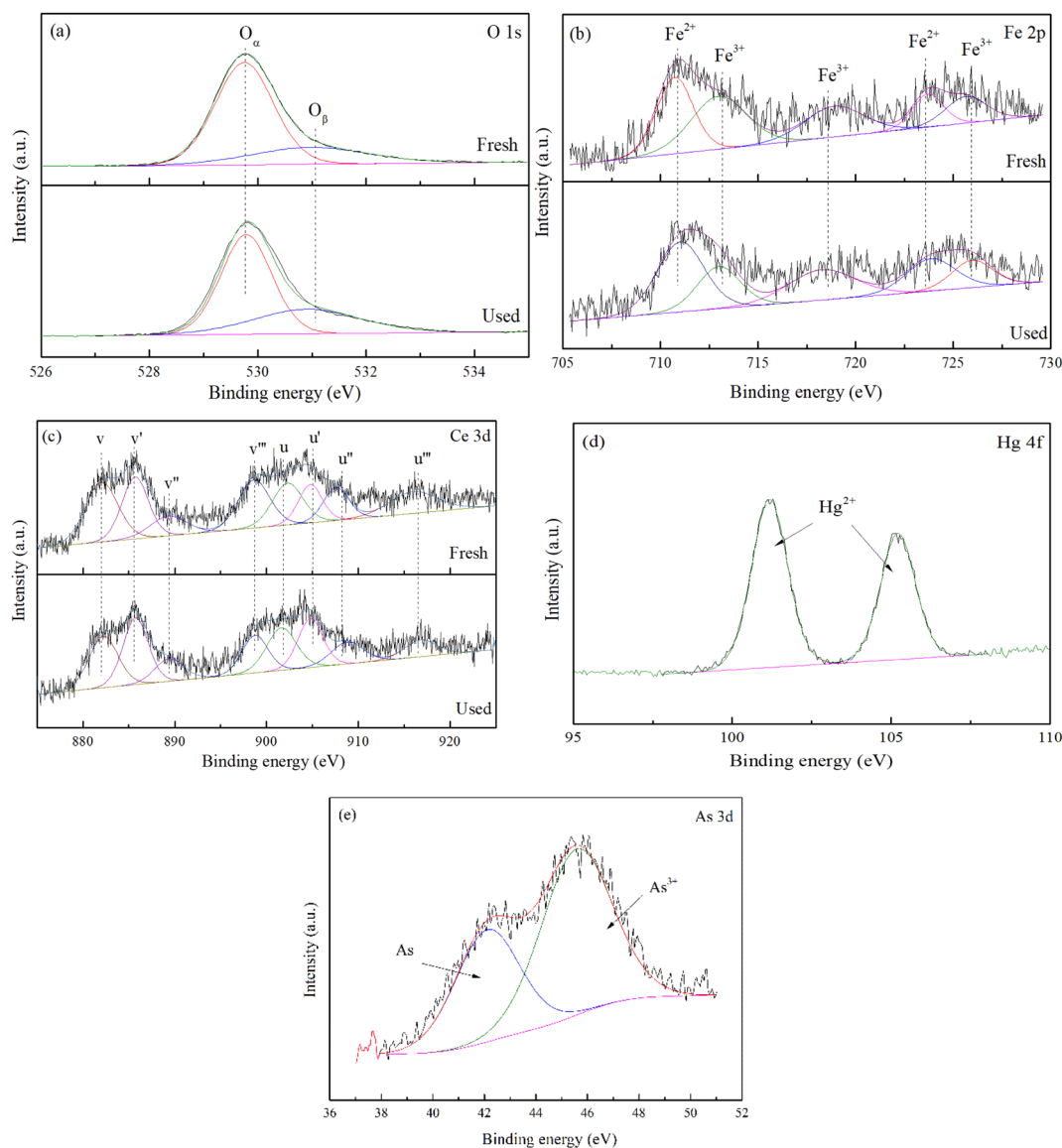

Fig. 8 XPS spectra of O 1s (a), Fe 2p (b), Ce 3d (c), Hg 4f (d) and As 3d (e) for fresh and used Fe_5Ce_5Ti catalysts.

Table 4   XPS results of the O 1s, Fe 2p, Ce 3d, Hg 4f and As 3d spectra and their elemental contents before and after the reaction

Groups/%	O 1s		Fe 2p		Ce 3d	
	O_α	O_β	Fe^{3+}	Fe^{2+}	Ce^{4+}	Ce^{3+}
Fresh	75.17	24.83	60.56	39.44	74.26	25.74
Used	65.80	34.20	50.54	49.55	65.90	34.10

Groups/%	Hg 4f	As 3d	
	Hg^{2+}	As	As^{3+}
Fresh	—	—	—
Used	100	38.16	61.84

the catalyst surface increased from 24.83% to 34.20%, indicating that chemisorbed oxygen can be supplemented from the gas phase.

The Fe 2p spectrum of the Fe_5Ce_5Ti catalyst is shown in Fig. 8(b). The characteristic peaks of the electron binding energies at 712.5 eV, 718.3 eV and 726.01 eV belong to Fe^{3+}, and the characteristic peaks at 710.45 eV and 724.04 eV represent Fe^{2+}.[42] The percentage content of Fe^{3+} and Fe^{2+} on the catalyst surface is shown in Table 4. Before the reaction, the electron binding energy of Fe 2p in the Fe_5Ce_5Ti catalyst is shifted to a higher energy direction, indicating that the electron cloud density near the Fe on the catalyst surface is relatively low, showing less free Fe in the system, and it was verified that the simultaneous doping of Ce and Fe produced an interaction. The strong induction effect of Ce on Fe caused the electron cloud distribution on the catalyst surface to shift towards Ce; this showed that the interaction between Fe and Ce gives the catalyst stronger redox capacity and improves the activity of the catalyst.[43] Compared with the Fe_5Ce_5Ti catalyst before the reaction, the Fe^{3+} content on the catalyst surface decreased from 60.56% to 50.54%, while the Fe^{2+} content increased from 39.44% to 49.55%. The results show that a part of Fe^{3+} participates in the reaction during the removal of Hg^0 and AsH_3 and is reduced to Fe^{2+}; that is, Fe^{3+} plays an important role in the catalytic oxidation reaction of Hg^0 and AsH_3.

The Ce 3d spectrum of the Fe_5Ce_5Ti catalyst is shown in Fig. 8(c) and can be divided into eight secondary peaks, with the characteristic peak of Ce $3d_{3/2}$ denoted as u, and the Ce $3d_{5/2}$ denoted as v. The characteristic peaks are u, u″, u‴, v, v″ and v‴ which belong to Ce^{4+}, and the electron binding energy positions are 900.8 eV, 907.1 eV, 916.6 eV, 882.5 eV, 889.0 eV and 898.5 eV, respectively. The characteristic peaks denoted as u′ and v′ are in the same position as Ce^{3+}, and the electron binding energy positions are 903.0 eV and 885.6 eV, respectively.[44] The ratios of Ce^{3+} and Ce^{4+} on the catalyst surface were denoted as $Ce^{3+}/(Ce^{3+} + Ce^{4+})$ and $Ce^{4+}/(Ce^{3+} + Ce^{4+})$, as shown in Table 4. The results show that the Ce on the surface of the Fe_5Ce_5Ti catalyst mainly exists in the form of Ce^{4+}; because of the coexistence of Ce^{3+} and Ce^{4+}, the redox electron pairs of Ce^{3+}/Ce^{4+} can be detected on the catalyst surface, which is conducive to the storage and release of oxygen on the catalyst surface, thus enhancing the redox performance of

the catalyst. The catalytic oxidation performance of Hg^0 and AsH_3 was enhanced.[45] After the reaction, the ratio of $Ce^{4+}/(Ce^{3+} + Ce^{4+})$ on the surface of the Fe_5Ce_5Ti catalyst decreased from 74.26% to 65.90%, illustrating that the presence of Ce^{4+} promoted the catalytic oxidation of Hg^0 and AsH_3. Meanwhile, Ce^{4+} promoted the transformation of Fe^{2+} to Fe^{3+}, which is beneficial for the simultaneous removal of Hg^0 and AsH_3.

The Hg 4f spectrum of the Fe_5Ce_5Ti catalyst after the reaction is shown in Fig. 8(d). Two obvious characteristic peaks were detected at electron binding energies of 101.2 eV and 105.2 eV, respectively, due to the characteristic peaks of Hg $4f_{7/2}$ and Hg $4f_{5/2}$ mercury oxide (HgO) species. The presence of Hg^0 was not observed on the surface of the catalyst after the reaction, which may be due to the desorption of Hg^0 during the reaction process or the volatilization of Hg^0 in the XPS test, resulting in the low concentration of Hg^0 on the surface. According to XPS analysis, mercury exists in the form of HgO on the surface of the Fe_5Ce_5Ti catalyst after the reaction.

The As 3d spectrum of the Fe_5Ce_5Ti catalyst after the reaction is shown in Fig. 8(e). The characteristic peak at the electron binding energy of 42.0 eV is attributed to elemental As, and the characteristic peak at the electron binding energy of 45.8 eV is As^{3+}, which is consistent with As_2O_3.[46,47] The results show that AsH_3 in the gas phase is oxidized into elemental As and As_2O_3, which were adsorbed on the surface of the catalyst.

3.3.   Catalyst regeneration performance evaluation

The service life and regeneration capacity of the Fe_5Ce_5Ti catalyst were investigated using the N_2 blowdown heating regeneration method. The reacted Fe_5Ce_5Ti catalyst was first reactivated by hot airflow for 3 h, then soaked and washed 4–5 times with deionized water. It was heated in a tube furnace with N_2 in the roasting temperature range for 1–2 h to regenerate the reacted Fe_5Ce_5Ti catalyst. At the end of heating, the tube furnace was turned off and the sample was allowed to cool to room temperature in the N_2 environment. The reaction conditions were as follows: 400 µg m^{-3} inlet concentration of Hg^0, 50 ppm inlet concentration of AsH_3, total gas flow rate of 800 mL min^{-1}, 1 vol% oxygen, and reaction temperature of 150 °C. The penetration adsorption capacities of the regenerated Fe_5Ce_5Ti catalysts for Hg^0 and AsH_3 removal reactions were lower than those of the fresh catalysts, as shown in Fig. 9, probably because the thermal regeneration destroyed the pore structure of the materials and reduced the active sites on the surface. This may be because the thermal regeneration destroyed the pore structure of the material and reduced the active sites on the surface. The catalyst was regenerated three times and still retained a penetration adsorption capacity of 1.773 mg g^{-1} for Hg^0 removal and 305.4 mg g^{-1} for AsH_3 removal. This indicates that the catalyst has excellent regeneration performance and service life. The previously reported Hg^0 and AsH_3 removal methods are summarized in Table 5.

3.4.   Mechanism discussion

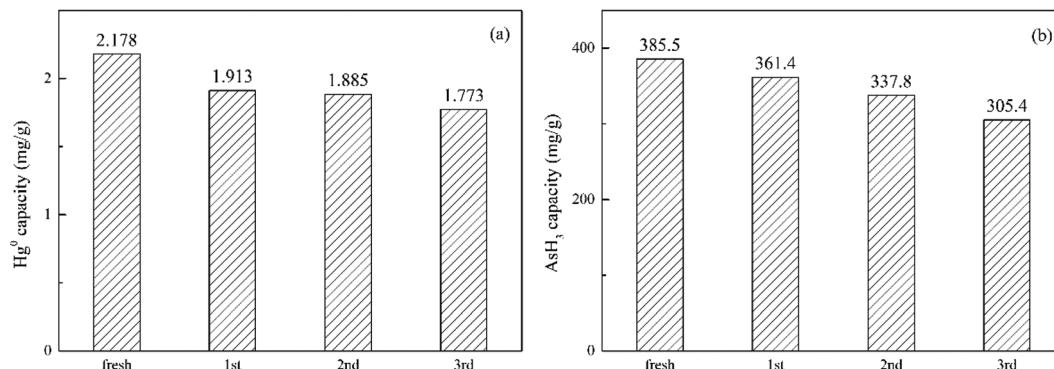According to the above experimental results and characterization analysis, the reaction mechanism of Fe–Ce-doped nano

Fig. 9 Hg^0 and AsH_3 adsorption tests after regeneration (total gas flow: 800 mL min^{-1}, catalyst filling capacity: 200 mg, Hg^0: 400 μg m^{-3}, AsH_3: 50 ppm, O_2: 1 vol%, CO: 80 vol%, reaction temperature: 150 °C).

Table 5 Summary of previous studies on Hg^0 and AsH_3 removal catalysts

Contaminant	Material	Removal rate/adsorption capacity (mg g^{-1})	Ref.
Hg^0	Active carbon	90%	25
Hg^0	Au	40–60%	48
Hg^0	RuO_2/rutile TiO_2	90%	49
Hg^0	TiO_2	90%	21
Hg^0	Ce_2-WO_3/TiO_2	95%	40
AsH_3	Cu-loaded active carbon	50%	50
AsH_3	CuO/TiO_2	534.3 mg g^{-1}	51

TiO_2 for the simultaneous removal of Hg^0 and AsH_3 in the yellow phosphorus flue gas was proposed and is shown in Fig. 10.

XPS characterized the chemical state of the major elements on the catalyst surface and the relative content of each element before and after the catalyst reaction. The characterization results showed that the pre-reaction lattice oxygen content was higher than the post-reaction content, while the chemisorbed oxygen pre-reaction content was lower than the post-reaction content, which indicates that the lattice oxygen is involved in the reaction. The content of Fe^{3+} and Ce^{4+} decreased before and after the catalyst reaction, while the content of Fe^{2+} and Ce^{3+} increased, which implies that Fe_2O_3 formed FeO, and CeO_2 was converted to Ce_2O_3 during the reaction. The reaction
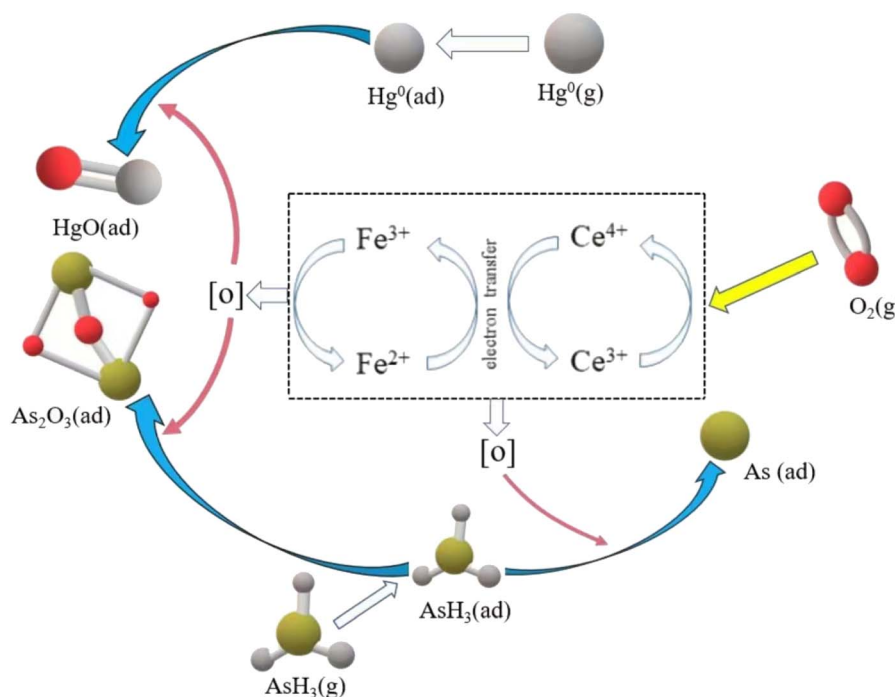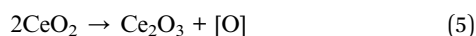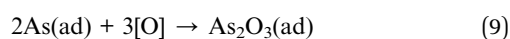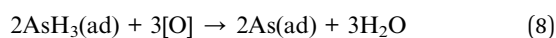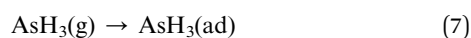

Fig. 10 Reaction mechanism for the removal of Hg^0 and AsH_3.

mechanism of the material was also judged in conjunction with previous studies,[6,18,46,51] making the mechanistic analysis more scientific.
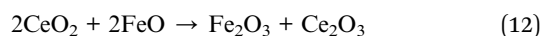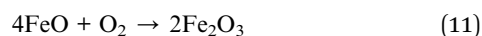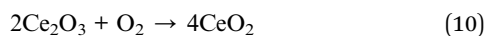
The removal mechanism of Hg^0 can be explained as follows: (1) the Hg^0 in the gas phase is attached to the active site on the surface of the catalyst by physical adsorption, and the adsorbed Hg^0 is formed. (2) The adsorbed e Hg^0 reacts with lattice oxygen provided by Fe–Ce bimetallic oxide to form HgO. The specific reaction is as follows:

$$Hg^0(g) \rightarrow Hg^0(ad) \tag{3}$$

$$Fe_2O_3 \rightarrow 2FeO + [O] \tag{4}$$

$$2CeO_2 \rightarrow Ce_2O_3 + [O] \tag{5}$$

$$Hg^0(ad) + [O] \rightarrow HgO(ad) \tag{6}$$
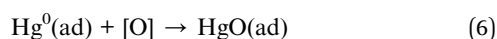
The reaction mechanism of AsH_3 can be explained as follows: (1) AsH_3 in the gas phase is adsorbed on the active site of the catalyst surface by physical adsorption, forming adsorbed AsH_3. (2) The adsorbed AsH_3 reacts with lattice oxygen provided by Fe–Ce bimetallic oxide and is oxidized to As. (3) As continues to react with lattice oxygen to form As_2O_3; the specific reactions are as follows:

$$AsH_3(g) \rightarrow AsH_3(ad) \tag{7}$$

$$2AsH_3(ad) + 3[O] \rightarrow 2As(ad) + 3H_2O \tag{8}$$

$$2As(ad) + 3[O] \rightarrow As_2O_3(ad) \tag{9}$$

The lattice oxygen consumed by the Fe–Ce bimetallic oxide can be supplemented by micro-oxygen in the simulated flue gas or provided by redox cycling between the Fe–Ce bimetallic oxide mixtures. The interaction of iron and titanium atoms can effectively disperse the active substances with strong oxidizing ability.[31] The valency of cerium oxide is lower than that of Fe^{3+}, so their compounds can effectively improve the oxygen storage and oxygen release properties of CeO_2, and the generation of a large number of cationic vacancies on the surface of CeO_2 can enhance its redox properties. The above experimental results and characterization analysis showed that the interaction between FeO and Ce_2O_3 promoted the catalytic oxidation reaction of Hg^0 and AsH_3; specific reactions are as follows:

$$2Ce_2O_3 + O_2 \rightarrow 4CeO_2 \tag{10}$$

$$4FeO + O_2 \rightarrow 2Fe_2O_3 \tag{11}$$

$$2CeO_2 + 2FeO \rightarrow Fe_2O_3 + Ce_2O_3 \tag{12}$$

4. Conclusions

In this paper, a catalyst, Fe_5Ce_5Ti, was developed for the simultaneous removal of Hg^0 and AsH_3 from yellow phosphorus flue gas. The catalyst showed the best oxidation capacity for Hg^0

and AsH_3 at the reaction temperature of 150 °C, the removal efficiency of Hg^0 was as high as 93.5%, and it also demonstrated a glorious performance in the removal of AsH_3. Under the optimal reaction conditions, the penetration adsorption capacity of the Fe_5Ce_5Ti catalyst for the removal of AsH_3 was 385.5 mg g^{-1} and for the removal of Hg^0 was 2.178 mg g^{-1}. O_2 in the flue gas also greatly contributed to the removal of Hg^0 and AsH_3, and the catalyst exhibited high Hg^0 and AsH_3 removal in conditions of 1% micro-oxygen. The oxidation mechanism of Hg^0 and AsH_3 was inferred from XPS analysis, and the catalytic oxidation reaction plays an important role in the removal of Hg^0 and AsH_3. Hg^0 and AsH_3 in the gas phase after the reaction were attached to the catalyst surface in the form of HgO and As_2O_3, and the Fe–Ce bimetallic oxides played a synergistic role in the reaction, which effectively enhanced the performance of the catalyst.

Author contributions

All authors contributed to the study conception and design. Writing – original draft preparation and conceptualization were performed by Huijuan Yu; conceptualization, funding acquisition, methodology and investigation were performed by Yingjie Zhang; writing – reviewing and editing were performed by Hong Quan; validation were performed by Dan Zhu; writing – reviewing and editing were performed by Shaohua Liao; data curation were performed by Cuiping Gao; writing – reviewing and editing were performed by Rongbin Yang; writing – reviewing and editing were performed by Zhenyu Zhang; writing – reviewing and editing were performed by Qiang Ma.

Conflicts of interest

There are no conflicts to declare.

Acknowledgements

References

1 S. Rodriguez, E. Cuevas, Y. Gonzalez, R. Ramos, P. M. Romero, N. Perez, X. Querol and A. Alastuey, Influence of sea breeze circulation and road traffic emissions on the relationship between particle number, black carbon, PM1, PM2.5 and PM2.5-10 concentrations in a coastal city, *Atmos. Environ.*, 2008, **42**(26), 6523–6534, DOI: **10.1016/j.atmosenv.2008.04.022**.

2 K. Cheng, Y. Wang, H. Tian, X. Gao, Y. Zhang, X. Wu, C. Zhu and J. Gao, Atmospheric Emission Characteristics and Control Policies of Five Precedent Controlled Toxic Heavy

Metals from Anthropogenic Sources in China, *Environ. Sci. Technol.*, 2015, **49**(2), 1206–1214, DOI: **10.1021/es5037332**.

3 H. Z. Tian, C. Y. Zhu, J. J. Gao, K. Cheng, J. M. Hao and K. Wang, Quantitative assessment of atmospheric emissions of toxic heavy metals from anthropogenic sources in china: historical trend, spatial distribution, uncertainties, and control policies, . *Atmospheric Chemistry and Physics*, 2015, **15**(17), 10127–10147, DOI: **10.5194/acpd-15-12107-2015**.

4 S. Wang, L. Zhang, L. Wang, Q. Wu, F. Wang and J. Hao, A review of atmospheric mercury emissions, pollution and control in China, *Front. Environ. Sci. Eng.*, 2014, **8**(5), 631–649, DOI: **10.1007/s11783-014-0673-x**.

5 H. Quan, H. J. Yu, X. Yang, D. P. Lv, X. Zhu and Y. C. Li, Long-term stabilization/solidification of arsenic-contaminated sludge by blast furnace slag-based cementitious material: functions of CaO and NaCl, *ACS Omega*, 2022, 7(36), 32631–32639, DOI: **10.1021/acsomega.2c04302**.

6 Y. J. Zhang, P. Ning, X. Q. Wang, L. L. Wang, Y. X. Ma, Q. Ma and Y. B. Xie, High efficiency of Mn-Ce-modified TiO_2 catalysts for the low-temperature oxidation of Hg0 under a reducing atmosphere, *Appl. Organomet. Chem.*, 2019, **33**(6), 4866, DOI: **10.1002/aoc.4866**.

7 H. Zhang, J. Zhao, Y. Fang, J. Huang and Y. Wang, Catalytic Oxidation and Stabilized Adsorption of Elemental Mercury from Coal-Derived Fuel Gas, *Energy Fuels*, 2012, **26**(3), 1629–1637, DOI: **10.1021/ef201453d**.

8 O. W., *The Global Mercury Assessment* UNEP. 2007.

9 M. Enrico, G. Le Roux, N. Maruszczak, L.-E. Heimbuerger, A. Claustres, X. Fu, R. Sun and J. E. Sonke, Atmospheric Mercury Transfer to Peat Bogs Dominated by Gaseous Elemental Mercury Dry Deposition, *Environ. Sci. Technol.*, 2016, **50**(5), 2405–2412, DOI: **10.1021/acs.est.5b06058**.

10 A. Dommergue, P. Martinerie, J. Courteaud, E. Witrant and D. M. Etheridge, A new reconstruction of atmospheric gaseous elemental mercury trend over the last 60 years from Greenland firn records, *Atmos. Environ.*, 2016, **136**, 156–164, DOI: **10.1016/j.atmosenv.2016.04.012**.

11 Z. L. Gong, X. F. Lu, M. S. Ma, C. Watt and X. C. Le, Arsenic speciation analysis, *Talanta*, 2002, **58**(1), 77–96, DOI: **10.1016/S0039-9140(02)00258-8**.

12 S. Das, G. K. Pradhan, S. Das, D. Nath and K. Das Saha, Enhanced protective activity of nano formulated andrographolide against arsenic induced liver damage, *Chem.-Biol. Interact.*, 2015, **242**, 281–289, DOI: **10.1016/j.cbi.2015.10.011**.

13 C. F. Huang, C. Y. Yang, D. C. Chan, C. C. Wang, K. H. Huang, C. C. Wu, K. S. Tsai, R. S. Yang and S. H. Liu, Arsenic Exposure and Glucose Intolerance/Insulin Resistance in Estrogen-Deficient Female Mice, *Environ. Health Perspect.*, 2015, **123**(11), 1138–1144, DOI: **10.1289/ehp.1408663**.

14 Y. Yao, V. Velpari and J. Economy, Design of sulfur treated activated carbon fibers for gas phase elemental mercury removal, *Fuel*, 2014, **116**, 560–565, DOI: **10.1016/j.fuel.2013.08.063**.

15 F. Ding, Y. C. Zhao, L. L. Mi, H. L. Li, Y. Li and J. Y. Zhang, Removal of Gas Phase Elemental Mercury in Flue Gas by Inorganic Chemically Promoted Natural Mineral Sorbents, *Ind. Eng. Chem. Res.*, 2012, **51**(7), 3039–3047, DOI: **10.1021/ie202231r**.

16 G. Li, S. Wang, Q. Wu, F. Wang, D. Ding and B. Shen, Mechanism identification of temperature influence on mercury adsorption capacity of different halides modified bio-chars, *Chem. Eng. J.*, 2017, **315**, 251–261, DOI: **10.1016/j.cej.2017.01.030**.

17 W. Xu, H. Wang, T. Zhu, J. Kuang and P. Jing, Mercury removal from coal combustion flue gas by modified fly ash, *J. Environ. Sci.*, 2013, **25**(2), 393–398, DOI: **10.1016/S1001-0742(12)60065-5**.

18 Y. J. Zhang, P. Ning, X. Q. Wang, L. L. Wang, Y. B. Xie, Q. Ma, R. Cao and H. Zhang, Simultaneous Removal of Elemental Mercury and Arsine from a Reducing Atmosphere Using Chloride and Cerium Modified Activated Carbon[J], *Ind. Eng. Chem. Res.*, 2019, **58**(51), 23529–23539, DOI: **10.1021/acs.iecr.9b04999**.

19 M. Jiang, Y. Bai, P. Ning, X. Huang, H. Liu and J. Fu, Adsorption removal of arsine by modified activated carbon, *Adsorption*, 2015, **21**(1–2), 135–141, DOI: **10.1007/s10450-015-9656-x**.

20 J. M. Kruk M, Gas Adsorption Characterization of Ordered Organic-Inorganic Nanocomposite Materials, *Chem. Mater.*, 2001, **13**(10), 3169–3183, DOI: **10.1021/cm0101069**.

21 H. Wang, S. Zhou, L. Xiao, Y. Wang, Y. Liu and Z. Wu, Titania nanotubes-A unique photocatalyst and adsorbent for elemental mercury removal, *Catal. Today*, 2011, **175**(1), 202–208, DOI: **10.1016/j.cattod.2011.03.006**.

22 F. Zhan, C. Li, G. Zeng, S. Tao, Y. Xiao, X. Zhang, L. Zhao, J. Zhang and J. Ma, Experimental study on oxidation of elemental mercury by UV/Fenton system, *Chem. Eng. J.*, 2013, **232**, 81–88, DOI: **10.1016/j.cej.2013.07.082**.

23 Y. Yuan, J. Zhang, H. Li, Y. Li, Y. Zhao and C. Zheng, Simultaneous removal of SO_2, NO and mercury using TiO_2-aluminum silicate fiber by photocatalysis, *Chem. Eng. J.*, 2012, **192**, 21–28, DOI: **10.1016/j.cej.2012.03.043**.

24 B. Podak, M. Brunetti, A. Lewis and J. Wilcox, Mercury binding on activated carbon, *Environ. Prog.*, 2006, **25**(4), 319–326, DOI: **10.1002/ep.10165**.

25 Y. Xie, C. Li, L. Zhao, J. Zhang, G. Zeng, X. Zhang, W. Zhang and S. Tao, Experimental study on Hg^0 removal from flue gas over columnar MnO_x-CeO_2/activated coke, *Appl. Surf. Sci.*, 2015, **333**, 59–67, DOI: **10.1016/j.apsusc.2015.01.234**.

26 R. Quinn, T. A. Dahl, B. W. Diamond and B. A. Toseland, Removal of arsine from synthesis gas using a copper on carbon adsorbent, *Ind. Eng. Chem. Res.*, 2006, **45**(18), 6272–6278, DOI: **10.1021/ie060176v**.

27 S. Poulston, E. J. Granite, H. W. Pennline, C. R. Myers, D. P. Stanko, H. Hamilton, L. Rowsell, A. W. J. Smith, T. Ilkenhans and W. Chu, Metal sorbents for high temperature mercury capture from fuel gas, *Fuel*, 2007, **86**(14), 2201–2203, DOI: **10.1016/j.fuel.2007.05.015**.

28 L. Zhao, C. Li, J. Zhang, X. Zhang, F. Zhan, J. Ma, Y. e. Xie and G. Zeng, Promotional effect of CeO_2 modified support on

V$_2$O$_5$-WO$_3$/TiO$_2$ catalyst for elemental mercury oxidation in simulated coal-fired flue gas, *Fuel*, 2015, **153**, 361–369, DOI: **10.1016/j.fuel.2015.03.001**.

29 H. Li, C. Wu, Y. Li and J. Zhang, CeO$_2$–TiO$_2$ Catalysts for Catalytic Oxidation of Elemental Mercury in Low-Rank Coal Combustion Flue Gas, *Environ. Sci. Technol.*, 2011, **45**(17), 7394–7400, DOI: **10.1021/es2007808**.

30 I. Atribak, N. Guillen, A. Bueno-López and A. García García, Influence of the physico-chemical properties of CeO$_2$−ZrO$_2$ mixed oxides on the catalytic oxidation of NO to NO$_2$, *Appl. Surf. Sci.*, 2010, **256**(24), 7760–7712, DOI: **10.1016/j.apsusc.2010.06.042**.

31 F. D. Liu, H. He, C. B. Zhang, W. P. Shan and X. Y. Shi, Mechanism of the selective catalytic reduction of NO$_x$ with NH$_3$ over environmental-friendly iron titanate catalyst, *Catal. Today*, 2011, **175**(1), 18–25, DOI: **10.1016/j.cattod.2011.02.049**.

32 S. B. Ghorishi, C. W. Lee, W. S. Jozewicz and J. D. Kilgroe, Effects of fly ash transition metal content and flue gas HCl/SO$_2$ ratio on mercury speciation in waste combustion, *Environ. Eng. Sci.*, 2005, **22**(2), 221–231.

33 S. Alikhanzadeh-Arani, M. Salavati-Niasari and F. Davar, Synthesis and characterization of the one-dimensional cuprate Sr$_2$CuO$_3$ nanoparticles prepared by modified sol–gel method, *High Temp. Mater. Proc.*, 2013, **32**(1), 1–6, DOI: **10.1515/htmp-2012-0166**.

34 Z. Liu, Y. Liu, B. Chen, T. Zhu and L. Ma, Novel Fe-Ce-Ti catalyst with remarkable performance for the selective catalytic reduction of NO$_x$ by NH$_3$, *Catal.: Sci. Technol.*, 2016, **6**, 6688–6696, DOI: **10.1039/C5CY02278A**.

35 J. Fan, L. Zhao, J. Yu and G. Liu, The effect of calcination temperature on the microstructure and photocatalytic activity of TiO$_2$-based composite nanotubes prepared by an *in situ* template dissolution method, *Nanoscale*, 2012, **4**(20), 6597–6603, DOI: **10.1039/C2NR32048G**.

36 J. Wu, X. Li, J. Ren, X. Qi, P. He, B. Ni, C. Zhang, C. Hu and J. Zhou, Experimental study of TiO$_2$ hollow microspheres removal on elemental mercury in simulated flue gas, *J. Ind. Eng. Chem.*, 2015, **32**, 49–57, DOI: **10.1016/j.jiec.2015.07.019**.

37 Y. Lin, X. Wang, J. Hao, P. Ning, G. Qu, Y. Ma and L. Wang, Improved Arsine Removal Efficiency Over MnO$_x$ Supported Molecular Sieves Catalysts *via* Micro-Oxygen Oxidation, *Energy Fuels*, 2017, **31**(9), 9752–9759, DOI: **10.1021/acs.energyfuels.7b01477**.

38 C. Su, C. M. Tseng, L. F. Chen, B. H. You, B. C. Hsu and S. S. Chen, Sol-hydrothermal preparation and photocatalysis of titanium dioxide, *Thin Solid Films*, 2006, **498**(1–2), 259–265, DOI: **10.1016/j.tsf.2005.07.123**.

39 J. Yu and B. Wang, Effect of calcination temperature on morphology and photoelectrochemical properties of anodized titanium dioxide nanotube arrays, *Appl. Catal., B*, 2010, **94**(3–4), 295–302, DOI: **10.1016/j.apcatb.2009.12.003**.

40 Q. Wan, L. Duan, K. He and J. Li, Removal of gaseous elemental mercury over a CeO$_2$-WO$_3$/TiO$_2$ nanocomposite in simulated coal-fired flue gas, *Chem. Eng. J.*, 2011, **170**(2–3), 512–517, DOI: **10.1016/j.cej.2010.11.060**.

41 M. Nasirian, C. F. Bustillo-Lecompte and M. Mehrvar, Photocatalytic efficiency of Fe$_2$O$_3$/TiO$_2$ for the degradation of typical dyes in textile industries: Effects of calcination temperature and UV-assisted thermal synthesis, *J. Environ. Manage.*, 2017, **196**, 487–498, DOI: **10.1016/j.jenvman.2017.03.030**.

42 P. C. J. Graat and M. A. J. Somers, Simultaneous determination of composition and thickness of thin iron-oxide films from XPS Fe 2p spectra, *Appl. Surf. Sci.*, 1996, **100**, 36–40, DOI: **10.1016/0169-4332(96)00252-8**.

43 C. Lv, J. Shi, Q. Tang and Q. Hu, Tetracycline Removal by Activating Persulfate with Diatomite Loading of Fe and Ce, *Molecules*, 2020, **25**, 5531, DOI: **10.3390/molecules25235531**.

44 L. Qu, C. Li, G. Zeng, M. Zhang, M. Fu, J. Ma, F. Zhan and D. Luo, Support modification for improving the performance of MnO$_x$-CeO$_y$/gamma-Al$_2$O$_3$ in selective catalytic reduction of NO by NH$_3$, *Chem. Eng. J.*, 2014, **242**, 76–85, DOI: **10.1016/j.cej.2013.12.076**.

45 W. Xu, Y. Yu, C. Zhang and H. He, Selective catalytic reduction of NO by NH$_3$ over a Ce/TiO$_2$ catalyst, *Catal. Commun.*, 2008, **9**(6), 1453–1457, DOI: **10.1016/j.catcom.2007.12.012**.

46 Y. Xie, L. Wang, P. Ning, X. Wang, Q. Wang, Y. Zhang and M. Wang, Superior activity of Ce-HZSM-5 catalyst for catalytic oxidation of arsine at low oxygen, *Appl. Organomet. Chem.*, 2019, **33**(3), 4745, DOI: **10.1002/aoc.4745**.

47 Y. J. Zhang, H. J. Yu, X. Q. Wang, L. L. Wang, Y. C. Li, D. P. Lv, D. Zhu and C. M. Tian, Simultaneous catalytic oxidation of elemental mercury and arsine over CeO$_2$(111) surface: a density functional theory study, *J. Mol. Model.*, 2022, **28**, 156, DOI: **10.1007/s00894-022-05153-4**.

48 Y. X. Zhao, M. D. Mann, J. H. Pavlish, B. A. F. Mibeck, G. E. Dunham and E. S. Olson, Application of gold catalyst for mercury oxidation by chlorine, *Environ. Sci. Technol.*, 2006, **40**(5), 1603–1608.

49 Z. Liu, V. Sriram and J.-Y. Lee, Heterogeneous oxidation of elemental mercury vapor over RuO$_2$/rutile TiO$_2$ catalyst for mercury emissions control, *Appl. Catal., B*, 2017, **207**, 143–152.

50 J. P. Baltrus, E. J. Granite, E. C. Rupp, D. C. Stanko, B. Howard and H. W. Pennline, Effect of palladium dispersion on the capture of toxic components from fuel gas by palladium-alumina sorbents, *Fuel*, 2011, **90**(5), 1992–1998.

51 X. Q. Wang, H. Q. Huang, Q. Q. Zhou, P. Ning, J. H. Cheng, Y. L. Lin, L. L. Wang and Y. B. Xie, High-Performance Arsine Removal Using CuO$_x$/TiO$_2$ Sorbents under Low-Temperature Conditions, *Energy Fuels*, 2018, **32**(6), 7035–7045.